

## Article

# Single Atomic Pt on SrTiO<sub>3</sub> Catalyst in Reverse Water Gas Shift Reactions

Yimeng Xing<sup>1</sup>, Mengyao Ouyang<sup>2</sup>, Lingling Zhang<sup>1</sup>, Ming Yang<sup>3</sup> , Xiaodong Wu<sup>1,4</sup> , Rui Ran<sup>4</sup>, Duan Weng<sup>1,4</sup>, Feiyu Kang<sup>1</sup> and Zhichun Si<sup>1,\*</sup>

- <sup>1</sup> Shenzhen International Graduate School, Tsinghua University, Shenzhen 518055, China; xingym18@mails.tsinghua.edu.cn (Y.X.); knowningmyself@163.com (L.Z.); wuxiaodong@tsinghua.edu.cn (X.W.); duanweng@tsinghua.edu.cn (D.W.); fykang@sz.tsinghua.edu.cn (F.K.)
- <sup>2</sup> Department of Chemical and Biological Engineering, Tufts University, Medford, MA 02155, USA; Mengyao.Ouyang@tufts.edu
- <sup>3</sup> Department of Chemical and Biomolecular Engineering, Clemson University, Clemson, SC 29634, USA; myang3@clemson.edu
- <sup>4</sup> School of Materials, Tsinghua University, Beijing 100084, China; ranr@tsinghua.edu.cn
- \* Correspondence: si.zhichun@sz.tsinghua.edu.cn; Tel.: +086-0755-86964076

**Abstract:** Copper catalysts were widely developed for CO<sub>2</sub> conversion, but suffered severe sintering at temperatures higher than 300 °C. Platinum was the most active and stable metal for RWGS reactions. However, the high price and scarcity of platinum restrained its application. Downsizing the metal particles can significantly improve the atom efficiency of the precious metal but the size effect of Pt on RWGS reactions was still unclear. In the present work, the single atomic Pt on SrTiO<sub>3</sub> was prepared using an impregnation leaching method, and the catalyst showed significant activity for an RWGS reaction, achieving a CO<sub>2</sub> conversion rate of 45%, a CO selectivity of 100% and a TOF of 0.643 s<sup>-1</sup> at 500 °C. The structures of the catalysts were characterized using XRD, STEM and EXAFS. Especially, the size effect of Pt in RWGS was researched using in situ FTIR and DFT calculations. The results reveal that single Pt atoms are the most active species in RWGS via a “-COOH route” while larger Pt cluster and nanoparticles facilitate the further hydrogenation of CO. The reaction between formate and H\* is the rate determination step of an RWGS reaction on a catalyst, in which the reaction barrier can be lowered from 1.54 eV on Pt clusters to 1.29 eV on a single atomic Pt.

**Keywords:** size effect; single Pt atoms; SrTiO<sub>3</sub>; reverse water gas shift (RWGS)



**Citation:** Xing, Y.; Ouyang, M.; Zhang, L.; Yang, M.; Wu, X.; Ran, R.; Weng, D.; Kang, F.; Si, Z. Single Atomic Pt on SrTiO<sub>3</sub> Catalyst in Reverse Water Gas Shift Reactions. *Catalysts* **2021**, *11*, 738. <https://doi.org/10.3390/catal11060738>

Academic Editor: Panagiotis G. Smirniotis

Received: 20 May 2021  
Accepted: 11 June 2021  
Published: 16 June 2021

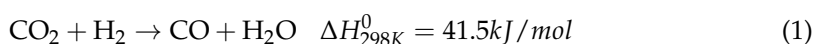
**Publisher's Note:** MDPI stays neutral with regard to jurisdictional claims in published maps and institutional affiliations.



**Copyright:** © 2021 by the authors. Licensee MDPI, Basel, Switzerland. This article is an open access article distributed under the terms and conditions of the Creative Commons Attribution (CC BY) license (<https://creativecommons.org/licenses/by/4.0/>).

## 1. Introduction

Global warming is becoming a rapid deterioration as a result of the huge release of CO<sub>2</sub> due to the extensive consumption of fossil energy. Upgrading CO<sub>2</sub> into more valuable products is considered as one of the most promising solutions for a CO<sub>2</sub>-neutral energy supply [1–4]. RWGS reaction (Equation (1)) is an important process for converting CO<sub>2</sub> to CO, which can be used as feedstock to produce value-added chemicals and synthetic fuels [5,6]. The key issue of RWGS is how to lower the activation energy barrier of high chemically stable CO<sub>2</sub> for obtaining high conversion rates and selectivity, and how to improve the long-term stability by reducing the carbon deposition and inhibiting the aggregation of active metal.



Supported noble metal catalysts are widely investigated for RWGS due to their high activities. However, the high prices and rare resources of these noble metals limit their application in large-scale production. Reducing the particle size to sub-nanoscale, such as single atomic site catalyst, may enhance the atom efficiency of noble metals. Single atomic metal catalysts are featured with isolated metal atoms anchored by the surrounding

coordination species of solid supports as single atomic active sites, which are different from Pt nanoparticles where the metal atoms are surrounded by the same metal atoms. Therefore, the catalytic performances and the stabilities of highly dispersed metal species are greatly influenced by the supports because the metal atoms are always coordinated by the atoms on the surface of the support (mainly surface defects or Lewis basic sites) [7–9]. Both reducible ( $\text{TiO}_2$  [10–16],  $\text{CeO}_2$  [17–20], etc.) and irreducible supports ( $\text{SiO}_2$  [21],  $\text{Al}_2\text{O}_3$  [16,22,23], zeolite [24],  $\text{MoS}_2$  [3],  $\text{Mo}_2\text{C}$  [25], etc.) have been adopted for loading highly dispersed Pt. For the Pt loading on a reducible support, the reverse water gas shift reaction was generally accepted as the redox mechanism via oxidation and reduction at the Pt sites and the metal/oxide interfaces [16]. The reactive area was also proposed over a Pt/ $\text{CeO}_2$  catalyst that Pt and ambient ceria (not solely the ceria on the Pt/ $\text{CeO}_2$  interface) surrounding the Pt center participated in the RWGS reaction [18]. In addition,  $\text{CO}_2$  can associatively adsorb on the surface defect sites to generate CO [18,26]. For the Pt catalysts loading on an irreducible support,  $\text{H}_2$  and  $\text{CO}_2$  are both activated on a metal center and the hydrogenation route may dominate the RWGS reaction [27]. The CO selectivity of a catalyst in  $\text{CO}_2$  hydrogenation reactions is closely related with the CO binding strength that may arise from the strong interactions (e.g., charge transfer) between the noble metal atoms and the oxide support and the particle size of Pt [11,26]. A strong PM-CO bond strength may lead to low CO selectivity. In similar results, a strong Co-CO bond strength was also reported to benefit the  $\text{CO}_2$  methanation activity over a Co/ $\text{CeO}_2$ - $\text{ZrO}_2$  catalyst [27]. However, the particle size effect of Pt on RWGS has seldom been reported.

Perovskite catalysts are becoming increasingly significantly advantageous in many reactions, such as dry reforming of methane [28], Suzuki couplings [29], water splitting [30], oxygen reduction [31] and automotive emissions control [32]. It is interesting that palladium (Pd) could reversibly move into and out of the perovskite lattice in the cycling between oxidative and reductive atmospheres. This movement helped to suppress the growth of metallic Pd particles [32]. A similar conclusion was also found on the Pd/ $\text{SrTiO}_3$  in Suzuki coupling reactions [29]. These results suggested that  $\text{SrTiO}_3$  may be a good support for a Pt catalyst in redox reactions. Furthermore, the surface alkaline-earth-metal Sr component was observed to enhance the adsorption and activation of  $\text{CO}_2$  [33]. Orlov and Chen et al. reported that Rh/ $\text{SrTiO}_3$  achieved good activity and CO selectivity for  $\text{CO}_2$  hydrogenation and the superior activity was suggested to originate from the cooperative effect between the highly dispersed sub-nanometer Rh clusters for the efficient dissociation of  $\text{H}_2/\text{C}_2\text{H}_6$  and the reconstructed  $\text{SrTiO}_3$  with oxygen vacancies for preferential adsorption/activation of  $\text{CO}_2$  [34]. Recently, the size effects of Pt particles in Pt/ $\text{CeO}_2$  catalysts among Pt single atoms, sub-nanoclusters (ca. 0.8 nm) and nanoparticles (3.8–9.3 nm) for the WGS were reported [35]. However, the size effects of Pt from single atomic to cluster in RWGS reactions have not been discussed; for example, the reaction routes and the states of intermediates on subnano metal catalysts may be different from nanocatalysts. In the present work, single atomic Pt and Pt nanoparticles were prepared using impregnation method followed by leaching. By means of in situ FTIR, the intermediate processes of Pt single atoms and Pt nanoparticles in an RWGS reaction were compared. Then, the reason for the different activities of Pt single atoms and Pt nanoparticles were explained from energy using DFT calculation.

## 2. Results and Discussions

### 2.1. Catalytic Performances

The catalytic performances of catalysts in RWGS reactions are shown in Figure 1. The true Pt content of catalysts determined using ICP-OES was as follows: Pt in Pt/ $\text{SrTiO}_3$  = 0.39% and Pt in Pt/ $\text{SrTiO}_3$ -L = 0.17%. Although the Pt content was significantly reduced by leaching, the Pt/ $\text{SrTiO}_3$ -L catalyst presented much higher  $\text{CO}_2$  conversions than pristine Pt/ $\text{SrTiO}_3$  at different temperatures. Table 1 shows the TOF of a Pt/ $\text{SrTiO}_3$ -L catalyst in an RWGS reaction at different temperatures. Chen [36] studied an RWGS reaction over the Pt/ $\text{CeO}_2$  catalyst; in his work, the best TOF of the sample with 1% Pt was  $0.056 \text{ s}^{-1}$  at

300 °C. The Pt/SrTiO<sub>3</sub>-L catalyst showed a much higher TOF than the Pt/CeO<sub>2</sub> catalyst; the main reason is the difference of metal dispersion. Large Pt particles make many Pt sites exist as invalid sites, so the TOF of Pt/CeO<sub>2</sub> catalyst is smaller than Pt/SrTiO<sub>3</sub>-L catalyst that loaded Pt in the form of a single atom and a cluster.

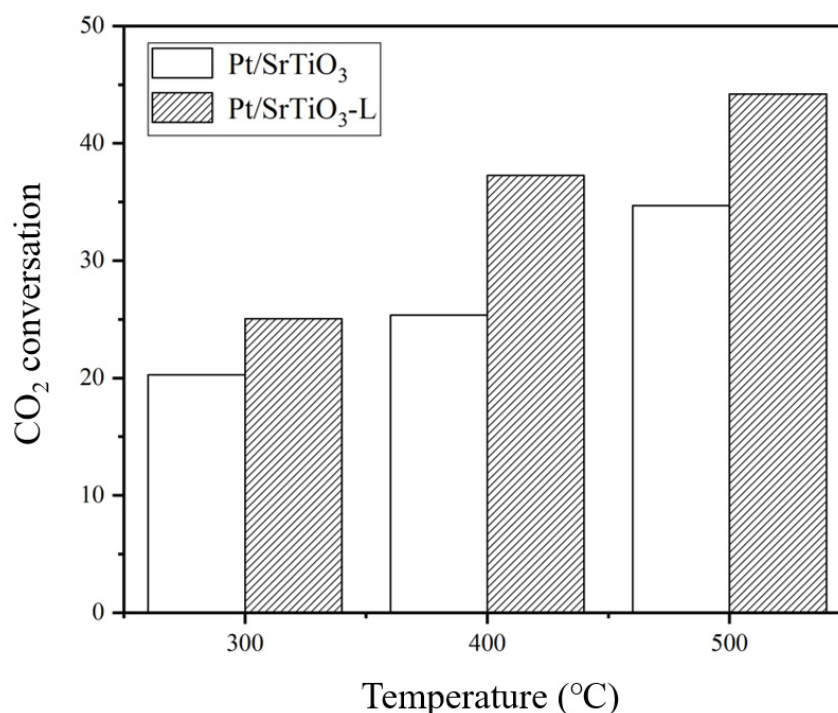


**Figure 1.** Catalytic performance of catalysts in RWGS at various temperatures.

**Table 1.** TOFs of Pt/SrTiO<sub>3</sub>-L catalyst in RWGS reaction at different temperatures.

	300	400	500
TOF (s <sup>-1</sup> )	0.154	0.455	0.643

## 2.2. Textural Properties

In order to further characterize the dispersion state of Pt species in a catalyst, high-resolution STEM images of the samples were taken. Figure 2a shows the HAADF-STEM images of a Pt/SrTiO<sub>3</sub> catalyst, in which the Pt nanoparticles are 2.72 nm in size. Figure 2b shows the HAADF-STEM images of a Pt/SrTiO<sub>3</sub>-L catalyst. Single atomic Pt and small Pt clusters composed of 2–8 atoms (atoms) can be seen. No Pt nano particles can be found on the Pt/SrTiO<sub>3</sub>-L catalyst.

The crystal phase of SrTiO<sub>3</sub> and the Pt/SrTiO<sub>3</sub> catalyst were measured using XRD, and the results are shown in Figure 2d. The synthesized SrTiO<sub>3</sub> is highly consistent with the standard diffraction pattern of SrTiO<sub>3</sub> (JCPDS# 35-0734). Pt related species cannot be found in all of the samples, indicating that the Pt species were well dispersed on SrTiO<sub>3</sub>. The extended X-ray absorption fine structure (EXAFS) measurements are shown in Figure 2e. Compared with the standard sample of Pt foil and PtO<sub>2</sub>, no obvious Pt-Pt bond was observed in either of the samples. The peak at 1.58 Å belonging to Pt-O coordination in the Pt/SrTiO<sub>3</sub>-L catalyst, was sharper than that of Pt/SrTiO<sub>3</sub>. The second peak at 2.8–3.2 Å, belonging to PtO<sub>2</sub> in Pt/SrTiO<sub>3</sub>-L catalyst, does not match the reference indicating that Pt species are mainly in sub-nanoscale and in highly undercoordinated state [37,38]. It should be mentioned that the EXAFS data were obtained ex situ. The valance state of Pt may not be the true state of Pt in RWGS reactions.

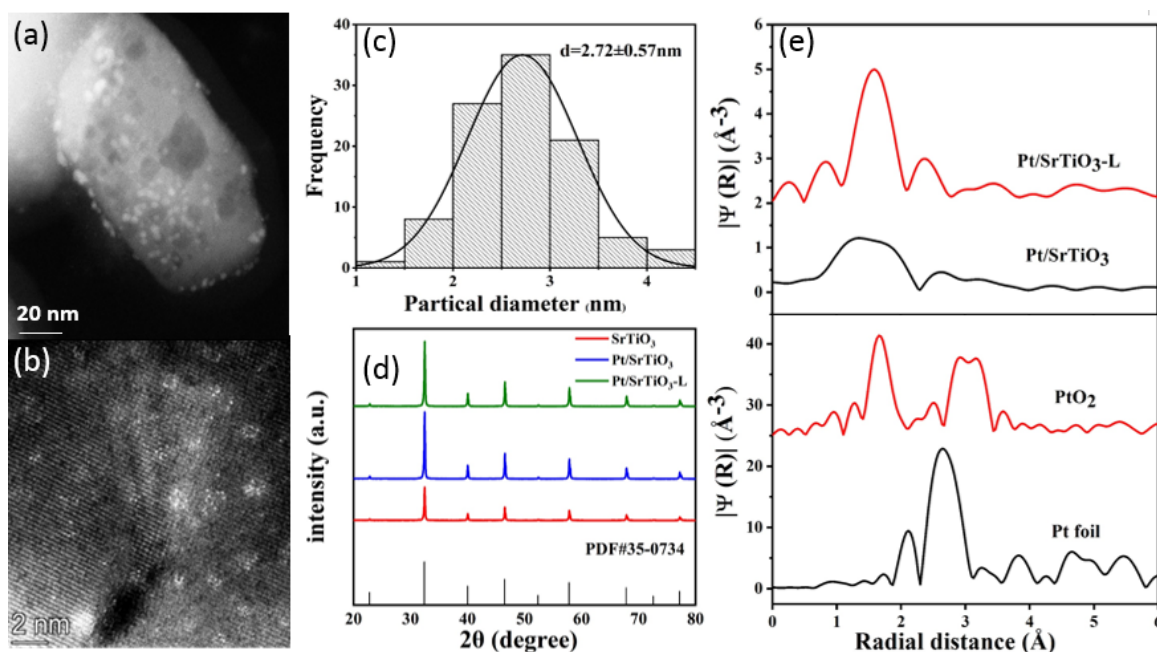


**Figure 2.** STEM photos of (a) Pt/SrTiO<sub>3</sub> and (b) Pt/SrTiO<sub>3</sub>-L, (c) size distribution of Pt particles on Pt/SrTiO<sub>3</sub> and (d) XRD profiles of catalysts, (e) Fourier transform of extended X-ray absorption fine structure (EXAFS) spectra of Pt L3 edge for Pt/SrTiO<sub>3</sub> and Pt/SrTiO<sub>3</sub>-L catalysts.

Table 2 shows the BET surface areas of the samples. After calcination at 1000 °C for 3 h, the specific surface area of SrTiO<sub>3</sub> was 17 m<sup>2</sup>/g. The Pt/SrTiO<sub>3</sub> and Pt/SrTiO<sub>3</sub>-L catalysts have a much smaller BET because loading Pt may block some of the pores in the catalyst and acid treatment may damage the pore structure of the catalyst.

**Table 2.** The BET results of samples.

Sample	SrTiO <sub>3</sub>	Pt/SrTiO <sub>3</sub>	Pt/SrTiO <sub>3</sub> -L
BET(m <sup>2</sup> /g)	17	11	9

### 2.3. H<sub>2</sub>-TPR

H<sub>2</sub>-TPR was used to characterize the redox properties of catalysts and the results are shown in Figure 3. There is only one H<sub>2</sub> consumption peak centered at 373 °C on SrTiO<sub>3</sub>, ascribed to the surface oxygen [39]. This peak is obviously widened on the Pt/SrTiO<sub>3</sub> catalyst arising from the activation effect of Pt on the oxide support surface [40,41]. As for the reduction in the Pt related species on the Pt/SrTiO<sub>3</sub> catalyst, two peaks at 68 and 201 °C, appearing that can be assigned to the reduction in the Pt nanoparticles and the oxygen on interfaces between Pt and the SrTiO<sub>3</sub> support. The significantly weakened H<sub>2</sub> consumption peak of Pt over Pt/SrTiO<sub>3</sub>-L catalyst is also located at 68 °C, but has a much smaller peak area, suggesting that a part of Pt atoms strongly interact with the support. Two overlapped H<sub>2</sub> consumption peaks at 300–400 °C of the Pt/SrTiO<sub>3</sub>-L catalyst can be ascribed to the reduction of the interface oxygen of Pt-O-SrTiO<sub>3</sub> and the surface oxygen of SrTiO<sub>3</sub> without interaction with Pt [42].

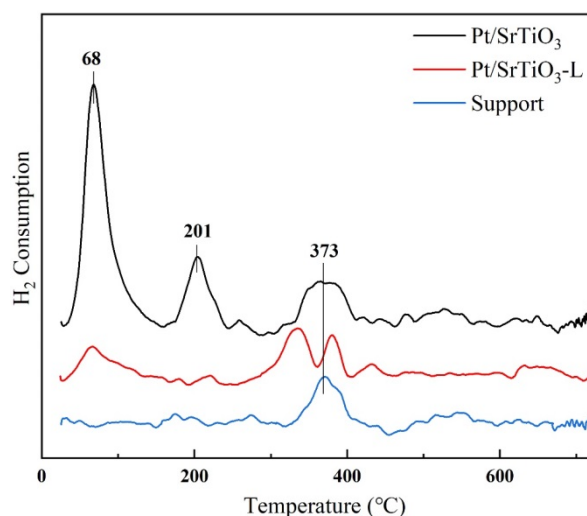


Figure 3. H<sub>2</sub>-TPR profiles of samples.

#### 2.4. In Situ FTIR

##### 2.4.1. CO<sub>2</sub> and H<sub>2</sub> Co-Adsorption on SrTiO<sub>3</sub> Support

Figure 4a,b shows the in situ FTIR of CO<sub>2</sub> and the H<sub>2</sub> co-adsorption on SrTiO<sub>3</sub>. The peaks at 2400–2300 cm<sup>-1</sup> are assigned to the linear adsorption of CO<sub>2</sub> [2,18,25]. The peaks at 1650–1680 cm<sup>-1</sup> and 1300 cm<sup>-1</sup> are assigned to asymmetric and symmetric stretching of CO<sub>2</sub><sup>δ-</sup>, respectively [18]. All of the species desorb with the elevation in the temperature. At temperatures higher than 200 °C, CO<sub>2</sub> molecules mainly physically and weakly adsorb on the SrTiO<sub>3</sub> support. The formate species (1559 cm<sup>-1</sup>) on SrTiO<sub>3</sub> can only be found at temperatures higher than 150 °C, indicating that SrTiO<sub>3</sub> also participates in the formation of formate intermediates.

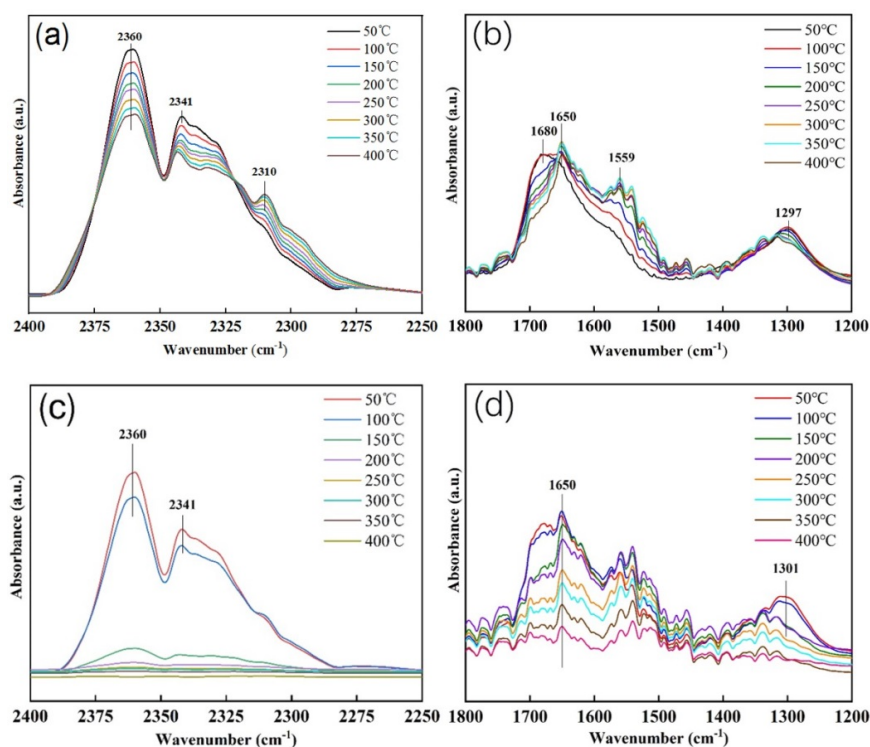


Figure 4. In-situ DRIFT spectra of SrTiO<sub>3</sub> support under CO<sub>2</sub> and H<sub>2</sub> co-adsorption (a,b); and pre-adsorption of CO<sub>2</sub> and then under H<sub>2</sub> purging (c,d).

When the in situ FTIR characterization was performed at first for CO<sub>2</sub> adsorption and then for purging by H<sub>2</sub>, the peaks of all of the CO<sub>2</sub> derived species reduced quickly and could be detected clearly at temperatures higher than 200 °C, suggesting that a bare SrTiO<sub>3</sub> support cannot adsorb and activate CO<sub>2</sub> efficiently.

#### 2.4.2. CO<sub>2</sub> and H<sub>2</sub> Adsorption on Pt/SrTiO<sub>3</sub> and Pt/SrTiO<sub>3</sub>-L

##### (1) CO<sub>2</sub> pre-adsorption and purging by H<sub>2</sub>

The in-situ DRIFT spectra of adsorbed species on the Pt/SrTiO<sub>3</sub> catalyst under CO<sub>2</sub> pre-adsorption and then purging by H<sub>2</sub>, are shown in Figure 5a–c. Physically adsorbed CO<sub>2</sub> molecules on both catalysts at 50 °C can be found as indicated by the peaks at 2200–2400 cm<sup>-1</sup>. The faster CO<sub>2</sub> desorption behavior on Pt/SrTiO<sub>3</sub> indicates that CO<sub>2</sub> adsorbing on Pt nanoparticles is more stable than those on Pt single atoms and clusters. The peaks at 2000–2100 cm<sup>-1</sup> were assigned to CO adsorbing atop metallic Pt atoms [43,44]. Both catalysts show similar behavior in CO adsorption with the elevation of temperature: the peak intensity becomes weaker because of desorption and the peak position redshifts due to a lower surface coverage. The peaks of Pt (CO) species on Pt/SrTiO<sub>3</sub>-L are much sharper and narrower than those on the Pt/SrTiO<sub>3</sub> catalyst, indicating the narrower size distribution of Pt species. The peaks at 1914–1929 cm<sup>-1</sup> are ascribed to CO on Pt nanoparticles or clusters [45]. The peaks in this region on a leached sample are significantly lower than those on pristine Pt/SrTiO<sub>3</sub>, indicating the removal of Pt nanoparticles by leaching. After excluding the influence of support and CO<sub>2</sub> products, the peaks at 1566–1539 and 1357–1395 cm<sup>-1</sup> can be assigned to the formate species produced in the co-adsorption reaction [2,13,25], as shown in Figure 5c,f. Compared with those on SrTiO<sub>3</sub> in Figure 4b,d, the signals of formate on Pt/SrTiO<sub>3</sub> and Pt/SrTiO<sub>3</sub>-L present at 50 °C, suggesting that Pt is the more active species, rather than the SrTiO<sub>3</sub> support for CO<sub>2</sub> hydrogenation to formate.

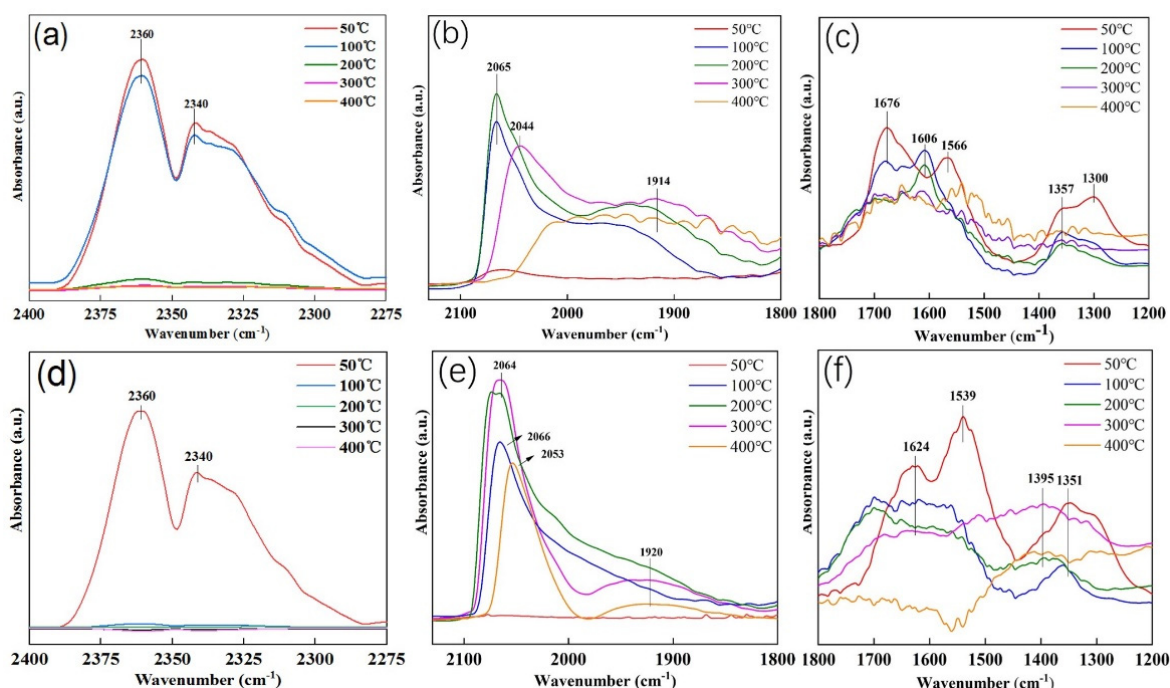


**Figure 5.** In-situ DRIFT spectra of species on catalyst pre-adsorbed by CO<sub>2</sub> and then purged by H<sub>2</sub>: Pt/SrTiO<sub>3</sub> catalyst (a–c) and Pt/SrTiO<sub>3</sub>-L catalyst (d–f).

##### (2) CO<sub>2</sub> and H<sub>2</sub> co-adsorption

The DRIFT spectra of the adsorbed species were collected under H<sub>2</sub> and CO<sub>2</sub> co-adsorption, and the results are shown in Figure 6. From Figure 6b,e, the Pt/SrTiO<sub>3</sub>-L

catalyst has stronger and narrower peaks of CO atop Pt at  $2071\text{ cm}^{-1}$  [44,45]. The peaks of CO on Pt clusters ( $1900\text{--}2000\text{ cm}^{-1}$ ) are very small. The Pt/SrTiO<sub>3</sub> catalyst has obviously broad peaks at  $2072\text{ cm}^{-1}$  (CO atop Pt atoms) and  $1927\text{ cm}^{-1}$  (CO on Pt nanoparticles), indicating the multiple CO-derived species on the Pt/SrTiO<sub>3</sub> catalyst. From Figure 6c,f, the peaks of formate ( $1800\text{--}1200\text{ cm}^{-1}$ ) on the Pt/SrTiO<sub>3</sub>-L catalyst are very weak suggesting that the formate species could convert to CO immediately. However, those species on the Pt/SrTiO<sub>3</sub> catalyst are still robust, even at  $400\text{ }^{\circ}\text{C}$ , indicating the strong adsorption of formate on the Pt nanoparticles.

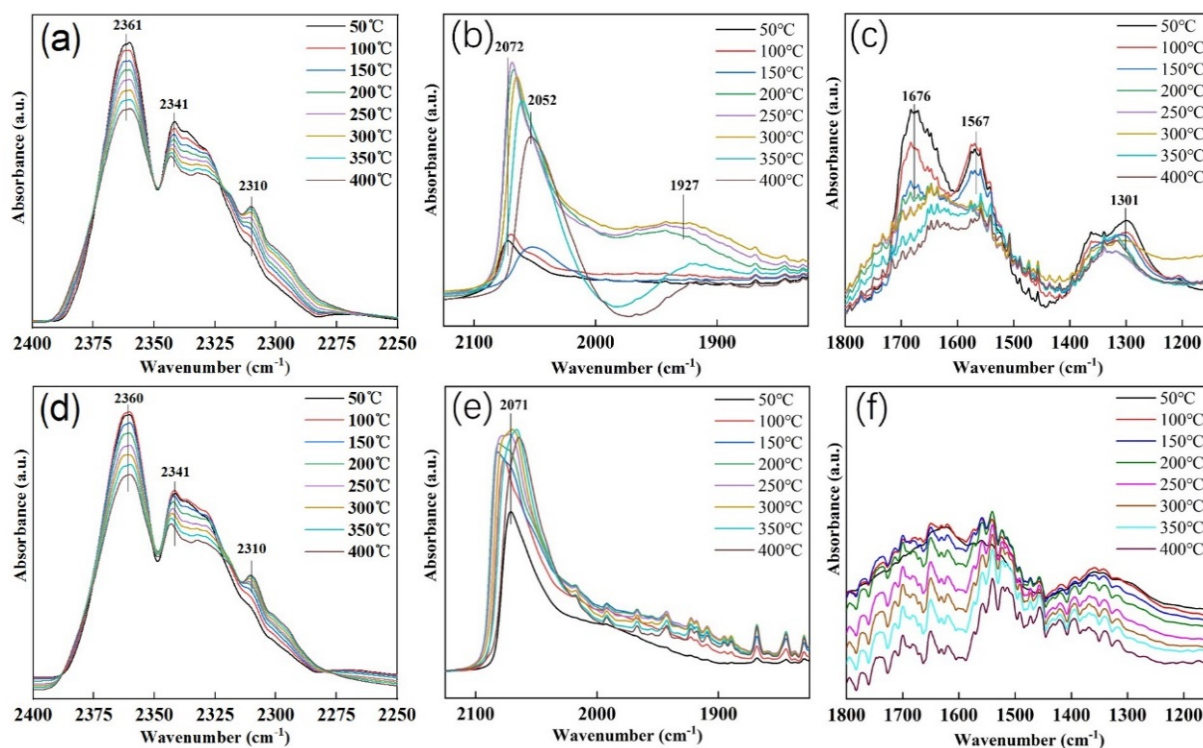


**Figure 6.** In-situ DRIFT spectra of species derived from H<sub>2</sub> and CO<sub>2</sub> co-adsorption on Pt/SrTiO<sub>3</sub> catalyst (a–c) and Pt/SrTiO<sub>3</sub>-L catalyst (d–f).

According to the above three groups of in situ FTIR results, the reaction path and gas activation site can be reasonably speculated. The SrTiO<sub>3</sub> support has no activity for an RWGS reaction, but intermediate species appeared on its surface when CO<sub>2</sub> was introduced. This shows that CO<sub>2</sub> is activated to generate intermediate species. After the addition of Pt, H<sub>2</sub> can be cracked on the surface of the metal, thereby making the catalyst active. As for the two catalysts, the Pt/SrTiO<sub>3</sub>-L catalyst showed a more obvious consumption of intermediate products than the Pt/SrTiO<sub>3</sub> catalyst, which might lead to the higher activity of the Pt/SrTiO<sub>3</sub>-L catalyst.

### 2.5. DFT Results and Reaction Mechanisms

According to the in situ FTIR results, sub-nano Pt is more active than Pt nano particles for the formation of formate and CO<sub>2</sub> can only be physically adsorbed on Pt/SrTiO<sub>3</sub>. Formate species may convert to CO immediately over the Pt/SrTiO<sub>3</sub>-L catalyst, which only has single Pt atoms and Pt clusters. To consolidate these conclusions, we further conducted DFT calculations to explore the possible reaction mechanism of RWGS over a catalyst.

The SrTiO<sub>3</sub> [110] surface (Figure 7) can provide six isolated sites to anchor six Pt atoms. While, further increasing the number of Pt atoms, there were not enough sites on the surface to isolate the Pt atoms, which made the formation of Pt clusters occur gradually. The Pt atoms tend to occupy the surface vacancy preferentially and hate to form Pt-Pt bonds when

the Pt content is low. From the in situ FTIR results, metallic Pt dominates the Pt species. Therefore, the Pt<sub>1</sub> single atom and Pt<sub>7</sub> metal cluster are used for the RWGS reaction as representatives. For comparison, we chose the models of the SrTiO<sub>3</sub> [110] surface loaded with isolated Pt atoms (Pt<sub>1</sub>/SrTiO<sub>3</sub>) and Pt<sub>7</sub> cluster (Pt<sub>7</sub>/SrTiO<sub>3</sub>) to investigate the size effect of Pt on the RWGS's performance. In the work of Chunyang Dong et al., the density functional theory of Pt nanoparticles was performed. The results show that it is difficult to form CO on Pt nanoparticles [46].

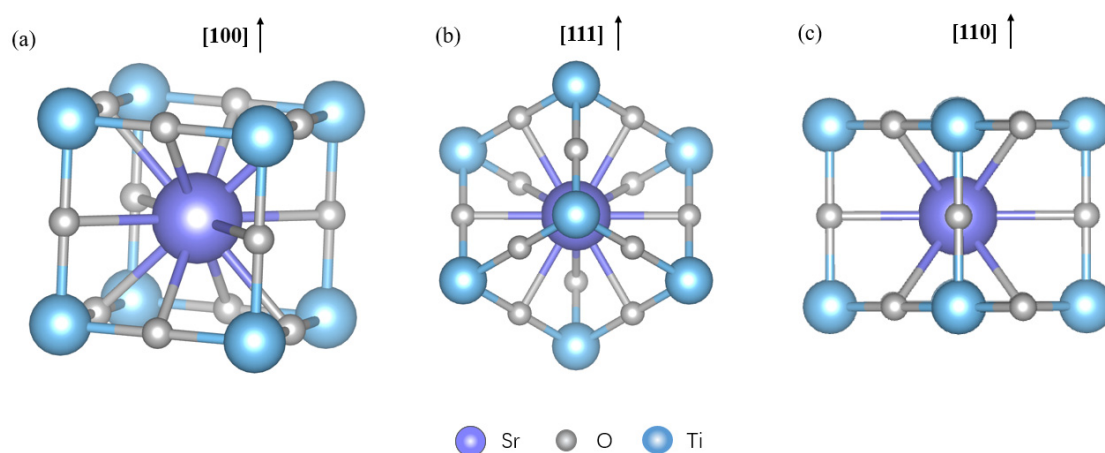


**Figure 7.** Structural representations of SrTiO<sub>3</sub>, the cubic perovskite structure. The [100] direction is highlighted in (a), while (b,c) shows a side view of the SrO<sub>3</sub>-terminated [111] and [110] surface, respectively.

We screened possible intermediates and reaction routes for CO<sub>2</sub> hydrogenation over Pt<sub>1</sub>/SrTiO<sub>3</sub> and Pt<sub>7</sub>/SrTiO<sub>3</sub>. The results are shown in Figure 8. On both surfaces, our calculations support the COOH intermediates mechanism in the RWGS reaction, CO<sub>2</sub> → COOH → CO, which is consistent with the results of in situ FTIR. Taking the reaction on Pt<sub>1</sub> as the example, the reaction starts by H<sub>2</sub> dissociated adsorption with an exothermic energy of 1.43 eV. Next, CO<sub>2</sub> shows a physical adsorption with an adsorption energy of −0.05 eV, suggesting the physically adsorption of CO<sub>2</sub> on Pt. In the presence of dissociated H atoms on Pt sites, the CO<sub>2</sub> can react with the H atoms to form COOH. The reaction barrier and reaction energy of this hydrogenation reaction over two catalysts are 0.72 (Pt<sub>1</sub>/SrTiO<sub>3</sub>) and 0.71 eV (Pt<sub>7</sub>/SrTiO<sub>3</sub>), respectively. The COOH intermediate over Pt<sub>1</sub>/SrTiO<sub>3</sub> then further reacts with a nearby H atom to produce CO and H<sub>2</sub>O with an energy barrier of 1.29 eV. The generated water desorbs into the gas phase, leaving behind the adsorbed CO molecule. However, this process on Pt<sub>7</sub>/SrTiO<sub>3</sub> needs much the higher energy of 1.54 eV, indicating that the reaction between formate and H\* is the rate determination step of the RWGS reaction and that Pt<sub>1</sub> is more active than Pt<sub>7</sub>. The strong adsorption of formate (in situ FTIR results) on the Pt cluster and nanoparticle may retard the reaction between the COOH intermediate and nearby H.

To understanding the CO behavior of desorption or hydrogenation on the catalysts, we further calculate the CO hydrogenation to CHO. The reaction barriers of CO hydrogenation are 1.88 and 1.07 eV on Pt<sub>1</sub>/SrTiO<sub>3</sub> and Pt<sub>7</sub>/SrTiO<sub>3</sub>, respectively. The high reaction barrier on Pt<sub>1</sub>/SrTiO<sub>3</sub> means that the generated CO molecule tends to desorb rather than hydrogenate. In contrast, on Pt<sub>7</sub>/SrTiO<sub>3</sub> the same reaction barrier of CO hydrogenation and RWGS indicates that the CO prefers to be hydrogenated to produce other hydrogenated products (e.g., CH<sub>2</sub>O, CH<sub>3</sub>OH, CH<sub>4</sub> etc.).

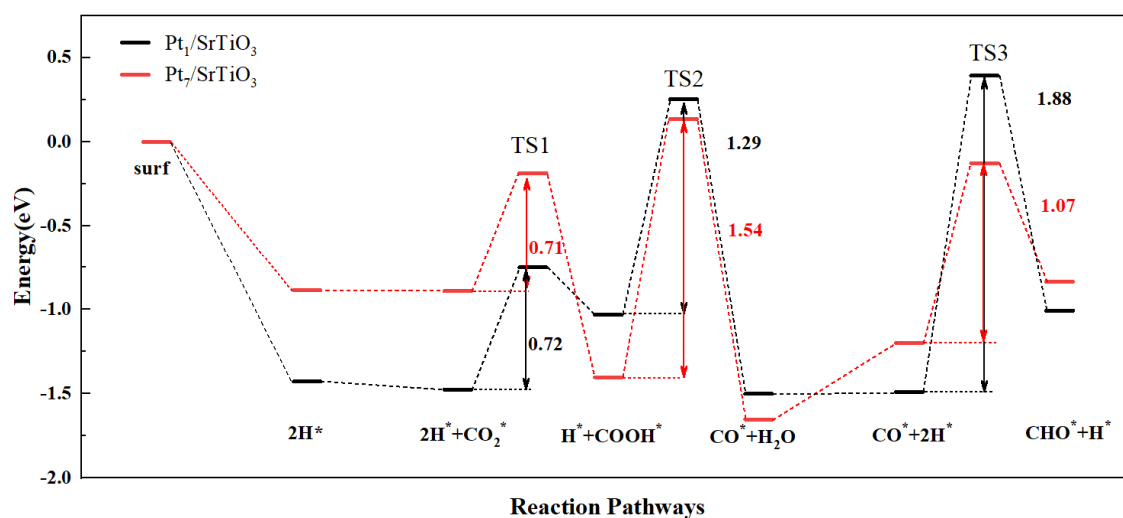


Figure 8. Calculated potential diagram by DFT for the redox mechanism of reverse water-gas shift reaction on Pt [111].

### 3. Experimental Method

#### 3.1. Catalyst Synthesis

The SrTiO<sub>3</sub> supports were prepared using a hydrothermal method. In 20 mL anhydrous ethanol, 4.39 g (0.015 mol) titanium isopropoxide (Ti[OCH(CH<sub>3</sub>)<sub>2</sub>]<sub>4</sub>, 97%, Sigma-Aldrich) (St Louis, MO, USA) was dissolved then 1.2 g of sodium hydroxide dissolved in 10 mL deionized water was added into the above solution. The obtained mixture was treated at 80 °C for 2 h to obtain precursor A. In 10 mL deionized water, 3.165 g of (0.015 mol) strontium nitrate was dissolved in 20 mL of deionized water, and then 1.2 g of sodium hydroxide was added dropwise to obtain precursor B. Precursors A and B were mixed and sealed in a Teflon container and kept at 150 °C for 2 h. The obtained product was centrifuged and washed several times with deionized water, then dried at 80 °C for 48 h. After that, the product was grinded to 80 mesh and heated at 1000 °C in a muffle furnace for 3 h to obtain well crystallized SrTiO<sub>3</sub>.

The Pt/SrTiO<sub>3</sub> catalyst was prepared using impregnation method. A certain amount of tetraammineplatinum dinitrate (H<sub>12</sub>N<sub>6</sub>O<sub>6</sub>Pt, Macklin, 99%, Newport Beach, CA, USA) was dissolved in 25 mL of an Ethylenediamine (Aladdin, 99%, Seattle, WA, USA) solution (0.001 g/mL of Pt) and then mixed with 5 g SrTiO<sub>3</sub> under stirring. After a 24-h immersion at room temperature, the catalyst was dried at 80 °C for 48 h. The obtained product was grinded to 80 mesh and heated at 350 °C at 5 °C/min for 3 h.

The Pt/SrTiO<sub>3</sub>-L catalyst was prepared by leaching Pt/SrTiO<sub>3</sub> catalyst. A total of 2.5 g of a Pt/SrTiO<sub>3</sub> catalyst was put into 50 mL HCl solution with a pH = 2 for 3 h. The product was centrifuged and washed several times with deionized water, then dried at 80 °C for 48 h.

#### 3.2. Characterizations

##### 3.2.1. Powder X-ray Diffraction (XRD)

XRD patterns were collected on a Bruker D8 Advance X-ray diffractometer (Billerica, MA, USA) using Cu K $\alpha$  ( $\lambda = 1.5406 \text{ \AA}$ ) radiation. Samples were tested on  $2\theta = 10^\circ\text{--}90^\circ$  at a scan rate of  $10^\circ \text{ min}^{-1}$ .

##### 3.2.2. BET and Inductively Coupled Plasma-Atomic Emission Spectrometry (ICP-OES)

Specific surface areas and pore structures of the catalysts were measured using ASAP 2020 Plus physisorption micromeritics (Micromeritics, Norcross, GA, USA). The true loading amount of Pt in a catalyst was measured on a Thermo IRIS Intrepid II (Waltham, MA, USA).

### 3.2.3. H<sub>2</sub>-Temperature-Programmed Reduction (H<sub>2</sub>-TPR)

Temperature-programmed-reduction (TPR) experiments were performed in a packed-bed flow microreactor (L = 22 inch, O.D. = 1/2 inch) in AutoChem II 2920 (Micromeritics). Samples of 50 mg mixed with 200 mg of SiO<sub>2</sub> were first pretreated under argon at 100 °C for 1 h. The sample then was cooled to 25 °C and heated from 25 °C to 700 °C in 10 °C/min under 10% H<sub>2</sub>/He.

### 3.2.4. Scanning Transmission Electron Microscopy (STEM)

Samples were characterized by FEI Tecnai G2 F30 Field Emission Transmission Electron Microscope (Hillsboro, OR, USA) and Titan ETEM Themis (Bangalore, India). The particle size distribution was obtained by measuring no less than 100 particles via ImageJ software (Shenzhen, China).

### 3.2.5. In Situ Fourier-Transformed Infrared Spectroscopy

In-situ DRIFTS experiments were performed on a Thermo Scientific Nicolet iS50. The following two kinds of intake experiments were carried out:

(1) The samples were firstly exposed to 10%CO<sub>2</sub> in He at room temperature for 30 min and then 10%H<sub>2</sub> in He treatment for 10 min.

(2) The samples were treated under a mixed gas of 5%H<sub>2</sub>+5%CO in He.

During these two processes, the IR spectra were collected at various temperatures under gas purging.

### 3.2.6. Density Functional Theory (DFT) Calculation Details

All of the density functional theory (DFT) calculations were performed using the Vienna ab-initio simulation package (VASP). The projector-augmented wave (PAW) method was used to represent the core-valence interaction [45,46]. The plane wave energy cutoff was set to 400 eV. The generalized gradient approximation (GGA) with the Perdew-Burke-Ernzerhof (PBE) exchange-correlation functional and local Hubbard term U correction was used in our calculations. The values of U are 3.5 for Ti. The Brillouin zone was sampled at Gamma point with the 1 × 1 × 1 k-point meshes for the SrTiO<sub>3</sub> [110] surface. The energy and force criterion for the convergence of the electron density are set at 10<sup>-5</sup> eV and 0.05 eV/Å, respectively. In order to research the size effect of Pt on SrTiO<sub>3</sub>, the size of single Pt atoms and clusters (several atoms) on the SrTiO<sub>3</sub> [110] surface were both calculated, considering the RWGS reaction on large Pt particles were studied extensively.

### 3.2.7. Extended X-ray Absorption Fine Structure

The k-edge extended X-ray absorption fine structure spectrum (EXAFS) of Pt was collected at the synchrotron radiation source (SSLS) center in Singapore, where the X-ray beam was monochromated with channel-cut Si [111] crystals. The k-edge absorption data of Pt was recorded in the transmission mode. Pt foil and PtO<sub>2</sub> were used as references. The working energy of the storage ring was 2.5 GeV, and the average electron current was less than 200 mA. The ATHENA module implemented in the IFEFFIT software package used to extract and process the acquired EXAFS data according to standard procedures. Using the Bessel window function, the k<sup>3</sup>-weighted Fourier transform (FT) of  $\chi(k)$  in R space was obtained in the range of 0–14.0 Å<sup>-1</sup>.

## 3.3. Activity Tests

All of the catalysts were performed in a fixed-bed reactor under atmospheric pressure. An electromagnetic flowmeter was used to control the flow rate of the feed gas. For the activity and stability test, 200 mg of a catalyst (80 mesh) mixed with 300mg of quartz sand (Macklin, AR, 50–80 mesh) was loaded in the center of a quartz tube (i.d. 10 mm). The gas flow of the reactants into the reactor was kept at 50 mL min<sup>-1</sup> (gas hourly space velocity = 6000 h<sup>-1</sup>). After purging by He for 30 min at 200 °C, the temperature of the tubular furnace was elevated to the reaction temperature for testing. Descending temperature

was used for the activity test. The gas products were analyzed using a gas chromatograph equipped with a flame ionization detector (FID) and a TCD (Fuli, GC9790plus, Taizhou, China). The RWGS activity of the catalyst was measured by the ratio of converted CO<sub>2</sub> to total CO<sub>2</sub>.

#### 4. Conclusions

In the present work, the single platinum atoms and nanoparticles on SrTiO<sub>3</sub> were prepared. The single atomic Pt catalyst showed excellent activity at temperatures higher than 300 °C, reaching a TOF of 0.643 s<sup>-1</sup> and 100% of CO selectivity at 500 °C in the RWGS reaction. The size effects of Pt in the RWGS reaction were researched using the DRIFTS and DFT methods. The results revealed that single Pt atoms have the highest activity and CO selectivity in RWGS via a “-COOH route”, while Pt metals of a larger particle size facilitate the further hydrogenation of CO. The reaction between formate and H<sup>\*</sup> is the rate determination step of the RWGS reaction over Pt/SrTiO<sub>3</sub>. The strong adsorption of formate (in situ FTIR results) on Pt clusters and nanoparticles may retard this reaction step.

**Author Contributions:** Y.X. and M.O. prepared and characterized the catalysts. Y.X. and Z.S. did the DFT calculation and wrote the manuscript. L.Z., M.Y., X.W., R.R., D.W. and F.K. helped in the characterization of catalysts. All authors have read and agreed to the published version of the manuscript.

**Funding:** This research was funded by the Strategic Emerging Industry Development Funds of Shenzhen (JCYJ20170817161720484) and the start-up funding provided by Clemson University.

**Data Availability Statement:** Not applicable.

**Conflicts of Interest:** The authors declare no conflict of interest.

#### References

1. Studt, F.; Sharafutdinov, I.; Abild-Pedersen, F.; Elkjær, C.F.; Hummelshøj, J.S.; Dahl, S.; Chorkendorff, I.; Nørskov, J.K. Discovery of a Ni-Ga Catalyst for Carbon Dioxide Reduction to Methanol. *Nat. Chem.* **2014**, *6*, 320–324. [[CrossRef](#)]
2. Li, H.; Wang, L.; Dai, Y.; Pu, Z.; Lao, Z.; Chen, Y.; Wang, M.; Zheng, X.; Zhu, J.; Zhang, W.; et al. Synergetic Interaction between Neighbouring Platinum Monomers in CO<sub>2</sub> Hydrogenation. *Nat. Nanotechnol.* **2018**, *13*, 411–417. [[CrossRef](#)] [[PubMed](#)]
3. Wang, L.; Zhang, W.; Zheng, X.; Chen, Y.; Wu, W.; Qiu, J.; Zhao, X.; Zhao, X.; Dai, Y.; Zeng, J. Incorporating Nitrogen Atoms into Cobalt Nanosheets as a Strategy to Boost Catalytic Activity toward CO<sub>2</sub> Hydrogenation. *Nat. Energy* **2017**, *2*, 869–876. [[CrossRef](#)]
4. Kattel, S.; Ramírez, P.J.; Chen, J.G.; Rodriguez, J.A.; Liu, P. Active Sites for CO<sub>2</sub> Hydrogenation to Methanol on Cu/ZnO Catalysts. *Science* **2017**, *355*, 1296–1299. [[CrossRef](#)] [[PubMed](#)]
5. Barroso Quiroga, M.M.; Castro Luna, A.E. Kinetic Analysis of Rate Data for Dry Reforming of Methane. *Ind. Eng. Chem. Res.* **2007**, *46*, 5265–5270. [[CrossRef](#)]
6. Baudouin, D.; Rodemerck, U.; Krumeich, F.; De Mallmann, A.; Szeto, K.C.; Ménard, H.; Veyre, L.; Candy, J.P.; Webb, P.B.; Thieuleux, C.; et al. Particle Size Effect in the Low Temperature Reforming of Methane by Carbon Dioxide on Silica-Supported Ni Nanoparticles. *J. Catal.* **2013**, *297*, 27–34. [[CrossRef](#)]
7. Millet, M.-M.; Algara-Siller, G.; Wrabetz, S.; Mazheika, A.; Girsdsies, F.; Teschner, D.; Seitz, F.-D.; Tarasov, A.; Levchenko, S.V.; Schlögl, R.; et al. Ni Single Atom Catalysts for CO<sub>2</sub> Activation. *J. Am. Chem. Soc.* **2019**, *141*, 2451–2461. [[CrossRef](#)]
8. Ji, S.; Chen, Y.; Wang, X.; Zhang, Z.; Wang, D.; Li, Y. Chemical Synthesis of Single Atomic Site Catalysts. *Chem. Rev.* **2020**, *120*, 11900–11955. [[CrossRef](#)]
9. Du, Y.; Sheng, H.; Astruc, D.; Zhu, M. Atomically Precise Noble Metal Nanoclusters as Efficient Catalysts: A Bridge between Structure and Properties. *Chem. Rev.* **2020**, *120*, 526–622. [[CrossRef](#)]
10. Tang, Y.; Asokan, C.; Xu, M.; Graham, G.W.; Pan, X.; Christopher, P.; Li, J.; Sautet, P. Rh Single Atoms on TiO<sub>2</sub> Dynamically Respond to Reaction Conditions by Adapting their Site. *Nat. Commun.* **2019**, *10*, 1–10. [[CrossRef](#)]
11. Matsubu, J.C.; Yang, V.N.; Christopher, P. Isolated Metal Active Site Concentration and Stability Control Catalytic CO<sub>2</sub> Reduction Selectivity. *J. Am. Chem. Soc.* **2015**, *137*, 3076–3084. [[CrossRef](#)] [[PubMed](#)]
12. Kattel, S.; Yan, B.; Chen, J.G.; Liu, P. CO<sub>2</sub> hydrogenation on Pt, Pt/SiO<sub>2</sub> and Pt/TiO<sub>2</sub>: Importance of synergy between Pt and oxide support. *J. Catal.* **2016**, *343*, 115–126. [[CrossRef](#)]
13. Chen, X.; Su, X.; Duan, H.; Liang, B.; Huang, Y.; Zhang, T. Catalytic Performance of the Pt/TiO<sub>2</sub> Catalysts in Reverse Water Gas Shift Reaction: Controlled Product Selectivity and a Mechanism Study. *Catal. Today* **2017**, *281*, 312–318. [[CrossRef](#)]
14. Kim, S.S.; Lee, H.H.; Hong, S.C. The Effect of the Morphological Characteristics of TiO<sub>2</sub> Supports on the Reverse Water–Gas Shift Reaction over Pt/TiO<sub>2</sub> Catalysts. *Appl. Catal. B Environ.* **2012**, *119–120*, 100–108. [[CrossRef](#)]

15. Matsubu, J.C.; Zhang, S.; DeRita, L.; Marinkovic, N.S.; Chen, J.G.; Graham, G.W.; Pan, X.; Christopher, P. Adsorbate-Mediated Strong Metal–Support Interactions in Oxide-Supported Rh Catalysts. *Nat. Chem.* **2017**, *9*, 120–127. [[CrossRef](#)]
16. Kim, S.S.; Lee, H.H.; Hong, S.C. A Study on the Effect of Support’s Reducibility on the Reverse Water–Gas Shift Reaction Over Pt Catalysts. *Appl. Catal. A Gen.* **2012**, *423–424*, 100–107. [[CrossRef](#)]
17. Guo, Y.; Mei, S.; Yuan, K.; Wang, D.-J.; Liu, H.-C.; Yan, C.-H.; Zhang, Y.-W. Low-Temperature CO<sub>2</sub> Methanation over CeO<sub>2</sub>-Supported Ru Single Atoms, Nanoclusters, and Nanoparticles Competitively Tuned by Strong Metal–Support Interactions and H-Spillover Effect. *ACS Catal.* **2018**, *8*, 6203–6215. [[CrossRef](#)]
18. Goguet, A.; Meunier, F.C.; Tibiletti, D.; Breen, J.P.; Burch, R. Spectrokinetic Investigation of Reverse Water–Gas-Shift Reaction Intermediates over a Pt/CeO<sub>2</sub> Catalyst. *J. Phys. Chem. B* **2004**, *108*, 20240–20246. [[CrossRef](#)]
19. Wang, L.; Khazaneh, M.T.; Widmann, D.; Behm, R. TAP Reactor Studies of the Oxidizing Capability of CO<sub>2</sub> on a Au/CeO<sub>2</sub> Catalyst—A First Step toward Identifying a Redox Mechanism in the Reverse Water–Gas Shift Reaction. *J. Catal.* **2013**, *302*, 20–30. [[CrossRef](#)]
20. Goguet, A.; Meunier, F.; Breen, J.; Burch, R.; Petch, M.; Faurghenciu, A. Study of the Origin of the Deactivation of a Pt/CeO Catalyst During Reverse Water Gas Shift (RWGS) Reaction. *J. Catal.* **2004**, *226*, 382–392. [[CrossRef](#)]
21. Fisher, I.A.; Bell, A.T. A Comparative Study of CO and CO<sub>2</sub> Hydrogenation over Rh/SiO<sub>2</sub>. *J. Catal.* **1996**, *162*, 54–65. [[CrossRef](#)]
22. Kwak, J.H.; Kovarik, L.; Szanyi, J. CO<sub>2</sub> Reduction on Supported Ru/Al<sub>2</sub>O<sub>3</sub> Catalysts: Cluster Size Dependence of Product Selectivity. *ACS Catal.* **2013**, *3*, 2449–2455. [[CrossRef](#)]
23. Wang, X.; Shi, H.; Kwak, J.H.; Szanyi, J. Mechanism of CO<sub>2</sub> Hydrogenation on Pd/Al<sub>2</sub>O<sub>3</sub> Catalysts: Kinetics and Transient DRIFTS-MS Studies. *ACS Catal.* **2015**, *5*, 6337–6349. [[CrossRef](#)]
24. Yang, X.; Su, X.; Chen, X.; Duan, H.; Liang, B.; Liu, Q.; Liu, X.; Ren, Y.; Huang, Y.; Zhang, T. Promotion Effects of Potassium on the Activity and Selectivity of Pt/Zeolite Catalysts for Reverse Water Gas Shift Reaction. *Appl. Catal. B Environ.* **2017**, *216*, 95–105. [[CrossRef](#)]
25. Zhang, X.; Zhu, X.; Lin, L.; Yao, S.; Zhang, M.; Liu, X.; Wang, X.; Li, Y.-W.; Shi, C.; Ma, D. Highly Dispersed Copper over β-Mo<sub>2</sub>C as an Efficient and Stable Catalyst for the Reverse Water Gas Shift (RWGS) Reaction. *ACS Catal.* **2016**, *7*, 912–918. [[CrossRef](#)]
26. Yan, B.; Wu, Q.; Cen, J.; Timoshenko, J.; Frenkel, A.; Su, D.; Chen, X.; Parise, J.B.; Stach, E.; Orlov, A.; et al. Highly Active Subnanometer Rh Clusters Derived from Rh-Doped SrTiO<sub>3</sub> for CO<sub>2</sub> Reduction. *Appl. Catal. B Environ.* **2018**, *237*, 1003–1011. [[CrossRef](#)]
27. Parastaev, A.; Muravev, V.; Osta, E.H.; Van Hoof, A.J.F.; Kimpel, T.F.; Kosinov, N.; Hensen, E.J.M. Boosting CO<sub>2</sub> Hydrogenation via Size-Dependent Metal–Support Interactions in Cobalt/Ceria-Based Catalysts. *Nat. Catal.* **2020**, *3*, 526–533. [[CrossRef](#)]
28. Topalidis, D.E.; Petrakis, A.; Ladavos, L.; Loukatzikou, P.J.; Pomonis, A. A Kinetic Study of Methane and Carbon Dioxide in-Terconversion over 0.5%Pt/SrTiO<sub>3</sub> Catalysts. *Catal. Today* **2007**, *127*, 238–245. [[CrossRef](#)]
29. Saputra, L.; Sato, T.; Kojima, T.; Hara, T.; Ichikuni, N.; Shimazu, S. Preparation of a Highly Stable Pd-Perovskite Catalyst for Suzuki Couplings via a Low-Temperature Hydrothermal Treatment. *ACS Omega* **2018**, *3*, 17528–17531. [[CrossRef](#)]
30. Lyu, H.; Hisatomi, T.; Goto, Y.; Yoshida, M.; Higashi, T.; Katayama, M.; Takata, T.; Minegishi, T.; Nishiyama, H.; Yamada, T.; et al. An Al-Doped SrTiO<sub>3</sub> Photocatalyst Maintaining Sunlight-Driven Overall Water Splitting Activity for over 1000 h of Constant Illumination. *Chem. Sci.* **2019**, *10*, 3196–3201. [[CrossRef](#)] [[PubMed](#)]
31. Jung, J.-I.; Jeong, H.Y.; Lee, J.-S.; Kim, M.G.; Cho, J. A Bifunctional Perovskite Catalyst for Oxygen Reduction and Evolution. *Angew. Chem.* **2014**, *126*, 4670–4674. [[CrossRef](#)]
32. Nishihata, Y.; Mizuki, J.I.; Akao, T.; Tanaka, H.; Uenishi, M.; Kimura, M.; Okamoto, T.; Hamada, N. Self-Regeneration of a Pd-perovskite Catalyst for Automotive Emissions Control. *Nat. Cell Biol.* **2002**, *418*, 164–167. [[CrossRef](#)] [[PubMed](#)]
33. Yuan, K.; Guo, Y.; Lin, Q.-L.; Huang, L.; Ren, J.-T.; Liu, H.-C.; Yan, C.-H.; Zhang, Y.-W. Size Effect-Tuned Water Gas Shift Reaction Activity and Pathway on Ceria Supported Platinum Catalysts. *J. Catal.* **2021**, *394*, 121–130. [[CrossRef](#)]
34. Chen, X.; Su, X.; Liang, B.; Yang, X.; Ren, X.; Duan, H.; Huang, Y.; Zhang, T. Identification of Relevant Active Sites and a Mechanism Study for Reverse Water Gas Shift Reaction over Pt/CeO<sub>2</sub> Catalysts. *J. Energy Chem.* **2016**, *25*, 1051–1057. [[CrossRef](#)]
35. Jeong, H.; Shin, D.; Kim, B.S.; Bae, J.; Shin, S.; Choe, C.; Han, J.W.; Lee, H. Controlling the Oxidation State of Pt Single Atoms for Maximizing Catalytic Activity. *Angew. Chem.* **2020**, *59*, 20691–20696. [[CrossRef](#)] [[PubMed](#)]
36. Wang, H.; Liu, J.-X.; Allard, L.F.; Lee, S.; Liu, J.; Li, H.; Wang, J.; Wang, J.; Oh, S.H.; Li, W.; et al. Surpassing the Single-Atom Catalytic Activity Limit through Paired Pt-O-Pt Ensemble Built from Isolated Pt1 Atoms. *Nat. Commun.* **2019**, *10*, 1–12. [[CrossRef](#)]
37. Puengjinda, P.; Muroyama, H.; Matsui, T.; Eguchi, K. Stability of Solid Oxide Fuel Cell Anodes Based on YST–SDC Composite with Ni Catalyst. *J. Power Sources* **2012**, *216*, 409–416. [[CrossRef](#)]
38. Peng, R.; Sun, X.; Li, S.; Chen, L.; Fu, M.; Wu, J.; Ye, D. Shape Effect of Pt/CeO<sub>2</sub> Catalysts on the Catalytic Oxidation of Toluene. *Chem. Eng. J.* **2016**, *306*, 1234–1246. [[CrossRef](#)]
39. Vayssilov, G.N.; Lykhach, Y.; Migani, A.; Staudt, T.; Petrova, G.P.; Tsud, N.; Skála, T.; Bruix, A.; Illas, F.; Prince, K.C.; et al. Support Nanostructure Boosts Oxygen Transfer to Catalytically Active Platinum Nanoparticles. *Nat. Mater.* **2011**, *10*, 310–315. [[CrossRef](#)]
40. Sola, A.C.; De La Piscina, P.R.; Homs, N. Behaviour of Pt/TiO<sub>2</sub> Catalysts with Different Morphological and Structural Characteristics in the Photocatalytic Conversion of Ethanol Aqueous Solutions. *Catal. Today* **2020**, *341*, 13–20. [[CrossRef](#)]
41. Toda, Y.; Hirayama, H.; Kuganathan, N.; Torrisi, A.; Sushko, P.; Hosono, H. Activation and Splitting of Carbon Dioxide on the Surface of an Inorganic Electride Material. *Nat. Commun.* **2013**, *4*, 2378. [[CrossRef](#)] [[PubMed](#)]

42. Jacobs, G.; Davis, B.H. Reverse Water-Gas Shift Reaction: Steady State Isotope Switching Study of the Reverse Water-Gas Shift Reaction using in Situ DRIFTS and a Pt/Ceria Catalyst. *Appl. Catal. A Gen.* **2005**, *284*, 31–38. [[CrossRef](#)]
43. Derita, L.; Dai, S.; Lopez-Zepeda, K.; Pham, N.; Graham, G.W.; Pan, X.; Christopher, P. Catalyst Architecture for Stable Single Atom Dispersion Enables Site-Specific Spectroscopic and Reactivity Measurements of CO Adsorbed to Pt Atoms, Oxidized Pt Clusters, and Metallic Pt Clusters on TiO<sub>2</sub>. *J. Am. Chem. Soc.* **2017**, *139*, 14150–14165. [[CrossRef](#)] [[PubMed](#)]
44. Dong, C.; Lian, C.; Hu, S.; Deng, Z.; Gong, J.; Li, M.; Liu, H.; Xing, M.; Zhang, J. Size-Dependent Activity and Selectivity of Carbon Dioxide Photocatalytic Reduction over Platinum Nanoparticles. *Nat. Commun.* **2018**, *9*, 1–11. [[CrossRef](#)] [[PubMed](#)]
45. Blöchl, P.E. Projector Augmented-Wave method. *Phys. Rev. B* **1994**, *50*, 17953–17979. [[CrossRef](#)]
46. Kresse, G.; Joubert, D. From Ultrasoft Pseudopotentials to the Projector Augmented-Wave Method. *Phys. Rev. B* **1999**, *59*, 1758–1775. [[CrossRef](#)]